ENGINEERING

Aligned 2D carbon nanotube liquid crystals for wafer-scale electronics

Katherine R. Jinkins[1], Sean M. Foradori[1], Vivek Saraswat[1], Robert M. Jacobberger[1], Jonathan H. Dwyer[2], Padma Gopalan[1,3], Arganthaël Berson[4], Michael S. Arnold[1]*

Semiconducting carbon nanotubes promise faster performance and lower power consumption than Si in field-effect transistors (FETs) if they can be aligned in dense arrays. Here, we demonstrate that nanotubes collected at a liquid/liquid interface self-organize to form two-dimensional (2D) nematic liquid crystals that globally align with flow. The 2D liquid crystals are transferred onto substrates in a continuous process generating dense arrays of nanotubes aligned within ±6°, ideal for electronics. Nanotube ordering improves with increasing concentration and decreasing temperature due to the underlying liquid crystal phenomena. The excellent alignment and uniformity of the transferred assemblies enable FETs with exceptional on-state current density averaging 520 μA μm^{-1} at only −0.6 V, and variation of only 19%. FETs with ion gel top gates demonstrate subthreshold swing as low as 60 mV $decade^{-1}$. Deposition across a 10-cm substrate is achieved, evidencing the promise of 2D nanotube liquid crystals for commercial semiconductor electronics.

INTRODUCTION

As field-effect transistors (FETs) continue to shrink and node scaling in conventional semiconductor devices becomes increasingly difficult, other next-generation materials must be investigated. Carbon nanotubes are one material candidate and are projected to outperform conventional semiconductors in FETs in terms of power efficiency, electrostatic gate control, and switching speed (*1*–*3*) but only when organized into aligned arrays. In addition, aligned arrays that can be deposited from solution or other low-temperature method might open the door to three-dimensional (3D) integrated circuits to increase FET areal density.

The fabrication of aligned arrays of nanotubes and other anisotropic particles from solution approaches has been investigated using shear (*4*, *5*), vacuum filtration (*6*), directed evaporation (*7*, *8*), dielectrophoresis (*9*), evaporative self-assembly (*10*, *11*), elastomeric release (*12*), dimension-limited self-alignment (*13*), DNA-directed assembly (*14*, *15*), Langmuir-Blodgett (*16*), and Langmuir-Schaefer (*17*) methods among others. However, more research is needed before any of these methods will be able to meet the needs of the semiconductor electronics industry. As examples, exceptionally large shear rates are needed to achieve deposition of nanotube films with even relatively poor quasi-alignment from bulk ink solutions (*4*), and evaporative self-assembly is a slow process that results in dense "coffee rings" of nanotubes that are difficult to efficiently gate electrostatically (*10*, *11*). In addition to alignment, especially important are achieving uniformity at the wafer scale and realizing partial monolayer coverage at an intermediate nanotube packing density (*1*) of roughly 100 μm^{-1} [because higher nanotube densities result in cross-talk effects that decrease performance, while lower densities yield lower currents (*18*)].

Broadly, the self-assembly of nanoparticles in solution at liquid interfaces offers an attractive route to fabricate supramolecular and 2D arrangements of nanostructures (*19*–*21*). This assembly is highly dynamic, enabling defects to be corrected quickly, as opposed to assembly and deposition directly on substrates. Nanoparticle adsorption at liquid/liquid interfaces occurs to minimize liquid/liquid interfacial energy, and the size of the nanoparticles, interfacial tension, and particle surface wettability all affect interface adsorption. When anisotropic particles, such as rods, collect at liquid/liquid interfaces, liquid crystal nematic assemblies can form (*22*, *23*).

Here, we demonstrate that single-walled carbon nanotubes that collect at a liquid/liquid interface can form 2D nematic liquid crystal assemblies, providing a route for accessing the nanotube array attributes needed for high-performance electronics. The 2D carbon nanotube assemblies are composed of individual domains of highly aligned nanotubes, and when the liquids are static, the domains lack global alignment. By tangentially flowing one liquid across the surface of the other, the domains orient with the direction of flow to form a globally ordered and structured interface. The assemblies are transferred to target substrates in a continuous process that enables the wafer-scale deposition of aligned and densely packed nanotubes.

Previously, locally aligned rafts of multiwalled carbon nanotubes (*24*, *25*) and relatively thick bundles or mats of randomly oriented single-walled nanotubes (*26*–*29*) have been deposited from liquid/liquid interfaces. However, these assemblies have lacked long-range order, and both multiwalled and disordered single-walled nanotube films are less desirable for electronics. Separately, the bulk liquid crystal assembly of nanotubes (i.e., not at a liquid/liquid interface) has been studied (*30*); however, bulk liquid crystals typically produce thick multilayer nanotube films with (*31*–*33*) or without (*34*, *35*) global alignment and rarely demonstrate submonolayer aligned nanotube arrays desired for FETs (*36*). It has also been hypothesized that 2D liquid crystal phenomena can affect nanotube organization at substrate/liquid interfaces (*37*).

Prior studies have also reported that stripes of aligned nanotubes can be deposited onto substrates during the spreading of sequential droplets of chloroform-based nanotube inks on an aqueous subphase (*38*, *39*). The roles of flow and liquid crystal assembly in this process,

---

[1]Department of Materials Science and Engineering, University of Wisconsin-Madison, 1509 University Ave., Madison, WI 53706, USA. [2]Department of Chemical and Biological Engineering, University of Wisconsin-Madison, 1415 Engineering Dr., Madison, WI 53706, USA. [3]Department of Chemistry, University of Wisconsin-Madison, 1101 University Ave., Madison, WI 53706, USA. [4]Department of Mechanical Engineering, University of Wisconsin-Madison, 1513 University Ave., Madison, WI 53706, USA.
*Corresponding author. Email: michael.arnold@wisc.edu

called floating evaporative self-assembly (FESA), are unknown. The excellent alignment, individualization, and packing of nanotubes in FESA films have enabled FETs with not only on-state current densities exceeding that of Si and GaAs devices (*40*, *41*) but also high-speed radio frequency devices (*42*). However, the drop-by-drop nature of deposition is irreproducible; is inherently difficult to scale [the best alignment has been demonstrated to occur across only 15 mm of a 100-mm wafer (*43*)], which limits FESA to the laboratory benchtop scale; and problematically yields stripes of aligned nanotubes that are either separated by randomly oriented nanotubes (*38*) or overlap (*43*).

Here, 2D nematic liquid crystals of nanotubes are obtained by applying continuous, well-defined ink layers with constant thickness and flow velocity to the surface of an aqueous subphase. The nanotubes collect at the interface, forming submonolayer 2D liquid crystals over a window of bulk ink concentrations ranging from 5 to 200 μg ml^{-1}. Sparse films of randomly oriented nanotubes and thicker multilayers of nanotubes are obtained at concentrations below and above this window, respectively. The 2D (as opposed to bulk) nature of the liquid crystalline assemblies is ideal for obtaining partial monolayer coverage at the intermediate nanotube packing density needed for high-performance electronics. As a benefit of the constant ink thickness and velocity, the 2D nanotube assemblies can be transferred to target substrates in a process that is scalable and continuous. We call this process 2D nematic tangential flow interfacial self-assembly (TaFISA). The excellent alignment in TaFISA nanotube arrays (within ±6°) and the continuous nature of the technique are substantial steps toward the uniformity and scalability that are needed to exploit carbon nanotubes in industrial electronics.

RESULTS

The apparatus for studying the liquid crystalline interfacial self-assembly of carbon nanotubes and subsequent deposition onto target substrates is shown in Fig. 1 (A to C). An ink of polymer-wrapped semiconducting carbon nanotubes (Fig. 1A) flows through a channel formed by a target substrate and a barrier suspended in a water subphase (Fig. 1B). Typical ink layer thicknesses in the channel depend on the ink volumetric flow rate and are between 0.1 and 0.5 mm, and the channel width (i.e., separation between substrate and barrier)

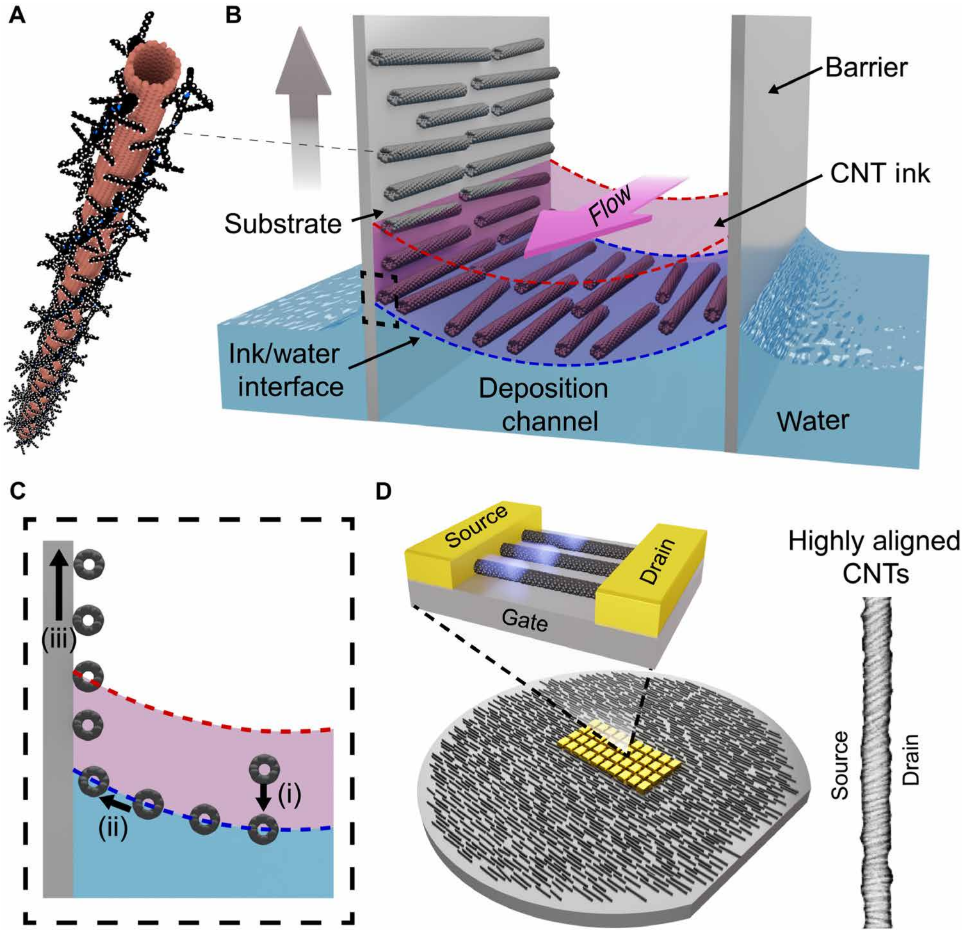

Fig. 1. Experimental apparatus for studying 2D liquid crystalline interfacial assembly in TaFISA. (**A**) Polymer-wrapped arc-discharge carbon nanotube (CNT) used in this work. (**B**) Experimental apparatus for TaFISA. (**C**) Magnified view of ink/water interface and alignment process shown in (B). In this process, nanotubes collect from the bulk ink at the ink/water interface (i) and deposit on the substrate (ii), yielding wafer-scale assemblies of aligned nanotubes (**D**) as the substrate is lifted (iii). The directed nature of TaFISA enables highly aligned nanotube FETs with uniform performance to be fabricated on the wafer scale. (D) Right: SEM image of aligned carbon nanotubes in FET channel of length 134 nm.

is roughly 3 mm. The characteristic time for evaporation of the ink layer is much greater than the characteristic transit time of the ink through the channel (calculation in the Supplementary Materials); therefore, evaporation is minor. The interfacial nanotube assemblies are transferred and deposited onto the substrate by translating the substrate and barrier together, through the flowing ink/water interface. The experimental setup is described in more detail in Materials and Methods, and specific experimental conditions for each figure are included in table S1. The directed and controlled ink flow enable uniform deposition across the wafer scale, and the exceptional alignment is ideal for FETs (Fig. 1D).

Evidence of 2D nematic assembly phenomena is shown in Fig. 2A (without added flow) and Fig. 2B (with flow). Even without flow, locally ordered domains of densely aligned nanotubes are deposited onto the substrate (observed underneath spurious random nanotubes), distinct from the disordered films of randomly oriented nanotubes that are created by dip-coating substrates into bulk solutions of nanotube ink without the 2D liquid/liquid interface (*44*, *45*). The approximate domain boundaries are outlined in black, and the characteristic orientation within each domain (termed the director) is marked by red arrows in Fig. 2A (green lines are traces of representative nanotubes in domains). Without flow, the orientation of each domain is different, and the nanotubes lack global order.

With flow, the domains globally align parallel to the direction of flow (Fig. 2B). On a 1.5 μm by 1.5 μm scale, the alignment is excellent with a half width at half maximum (HWHM) in an angular spread of 5.7° (calculated order parameter = 0.90). This narrow spread is comparable to the excellent alignment observed in the striped regions of FESA (Fig. 2C); however, the TaFISA arrays are continuously deposited across the substrate, without the randomly oriented regions of FESA films. The continuous, uniform nature of TaFISA, both without and with flow, is evidenced by Raman spectroscopy maps of relative nanotube density in Fig. 2 (D and E, respectively), in comparison to striped FESA films in Fig. 2F.

As discussed further below, the addition of flow enables aligned arrays of carbon nanotubes to be deposited on the wafer scale (Fig. 2, G to I). Shown in Fig. 2G is an optical image of a 10-cm-wide wafer piece with TaFISA-aligned nanotubes deposited across it. Overlaid are Raman spectroscopy maps of carbon nanotube density, confirming nanotube deposition and alignment (Fig. 2I) across the region of developed flow (~60% of the wafer).

With increasing flow velocity, the local directors become more aligned with each other—even over large areas—as characterized and quantified in Fig. 3. Large (greater than 6 μm by 6 μm) scanning electron microscopy (SEM) images of assemblies deposited using a volumetric flow rate of 0, 1, and 4 ml min^{-1} are compared in Fig. 3 (A to C, respectively). 2D fast Fourier transforms are used to quantify and map local director orientation as shown in red (*46*). This mapping is conducted on six different areas of each sample (see figs. S1 and S2), and cumulative distributions of director orientations are shown in Fig. 3 (D to F).

Without flow, the directors are oriented at all angles, showing a lack of global ordering but with local ordering in domains that is 3 to 30 μm in extent (Fig. 3, A and D). With increasing flow (1 ml min^{-1}), a clear global preferential orientation appears in the director distribution with an HWHM of 37.3° (Fig. 3, B and E), and at high flow (4 ml min^{-1}), the distribution narrows, with an HWHM of 16.1° centered around 0°, the direction of flow (Fig. 3, C and F). The spread in director orientation in TaFISA films (Fig. 3F, blue distribution) reduces at high flow rates, nearing that of the local nanotube orientation histogram (Figs. 2B, inset, and 3F, dashed black line).

These trends are moreover qualitatively observed over an even larger scale (1.4 mm by 1.4 mm) in the polarized optical microscopy (POM) images in Fig. 3 (G to I), where bright yellow corresponds to nanotubes aligned with the flow direction (horizontal) and darker regions correspond to misaligned nanotubes. The nanotube density can also be smaller in these darker regions (fig. S3). Without flow, the POM images are composed of roughly equal amounts of bright and dark regions, indicating a lack of global uniformity and alignment (Fig. 3G). At intermediate flow (1 ml min^{-1}), the POM images become more homogeneous, and at a high flow (4 ml min^{-1}), the POM images are nearly uniform in intensity, with all nanotube domains oriented roughly with the flow direction and deviation limited to highly localized regions.

An SEM image of one of these highly localized darker regions is shown in Fig. 3H inset. These nanotube arrangements correspond to liquid crystal defects or disclination lines, i.e., locations where the director cannot be determined. Liquid crystal defects are characterized with a charge related to the direction and number of times the director rotates 2π after traversing a circle around the defect. The liquid crystal defects in Fig. 3H inset have charges of $-^1/_2$ (blue) and $+^1/_2$ (red). The uniformity at a flow rate of 8 ml min^{-1} is similar to that at 4 ml min^{-1}, with marginal increase in defects; however, increasing the flow rate to 16 ml min^{-1} considerably deteriorates ordering, introduces more substantial defects, and results in incomplete coverage (fig. S4). Thus, there is a trade-off between shear-inducing alignment of the 2D liquid crystalline domains and assembly degradation. Possible factors that degrade the film alignment and uniformity are flow instability and director turbulence (*47*, *48*).

Ordering in TaFISA films markedly improves with increasing concentration (Fig. 4, A to C), indicating the importance of collective interactions among nanotubes and further evidencing underlying lyotropic liquid crystal phenomena. At low bulk ink concentrations of 0.1 μg ml^{-1} (Fig. 4A), nanotubes that are poorly aligned and at a low density are deposited, despite the high flow rate (4 ml min^{-1}). Collective interactions begin to create local order as the concentration increases to 5 μg ml^{-1} (Fig. 4B) and then reach a high degree of order at a concentration of 100 μg ml^{-1} (Fig. 4C). At higher ink concentrations, such as 200 μg ml^{-1}, the size of the defect regions increases (fig. S6), possibly because of increased heterogeneity within the ink caused by nanotube bundles and aggregates that form at elevated concentrations (*34*, *49*–*51*). The linear packing density of resolvable rod-like objects increases with bulk ink concentration, reaching 50 ± 4 μm^{-1} at an ink concentration of 100 μg ml^{-1} near the intermediate density needed for carbon nanotube–based FETs (Fig. 4, C and D). Note that the density of nanotubes is likely higher than measured because of undercounting of individual nanotubes that are spaced by less than the resolution of the SEM.

The concentration dependence data inform about the mechanism and dimensionality of the underlying phenomena. In bulk solution, Onsager's rigid rod theory predicts the onset of liquid crystal assembly at a concentration of 13 mg ml^{-1} (considering the dimensions of nanotubes used here, see calculation in the Supplementary Materials) (*52*, *53*). Experimental work has observed liquid crystal behavior in bulk nanotube solutions at concentrations as much as an order of magnitude below the prediction of Onsager's theory (*33*). In contrast, liquid crystal behavior emerges at markedly lower concentrations in TaFISA, with optimal ordering obtained at 100 μg ml^{-1} and

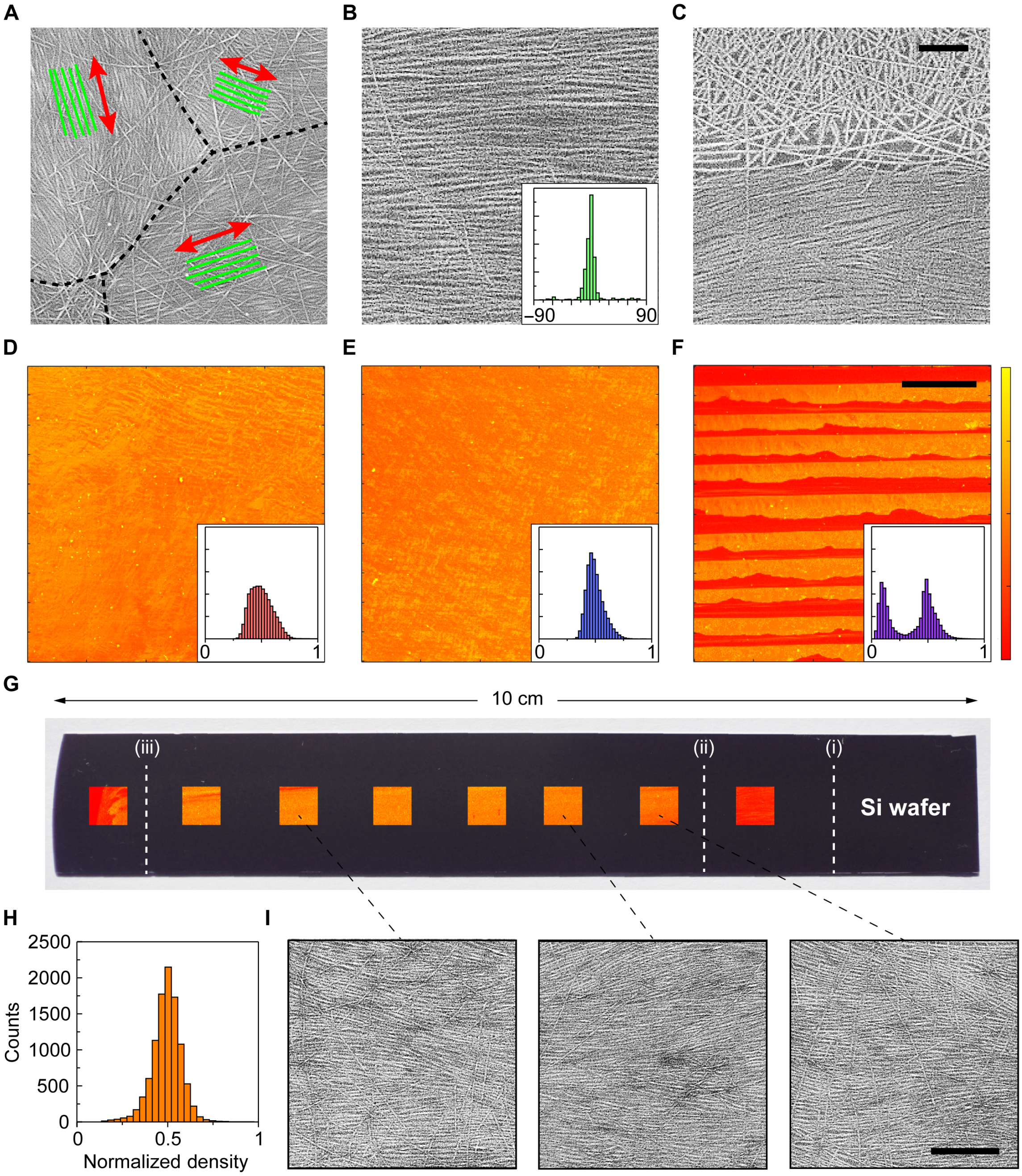

Fig. 2. Effect of flow on TaFISA alignment and demonstration of TaFISA alignment across a 10-cm-wide SiO_2/Si wafer piece. (**A** and **B**) SEM of TaFISA films obtained without flow and with flow. The inset in (B) is a histogram (manually extracted) of orientation angle, weighted by nanotube length. The *x* axis varies from −90° to 90°. (**C**) SEM of FESA film. The scale bar in (C) is 250 nm and applies to (A) to (C). (**D** to **F**) Raman spectroscopy maps of relative carbon nanotube density from each respective film in (A) to (C). Color scale bar on the right of (F) is linear and applies to (D) to (G). The scale bar in (F) is 250 μm and applies to (D) to (F). Histograms of nanotube density from the Raman maps are included as insets in each panel. The *x* axis of each histogram quantifies nanotube density, normalized so that the mode of each distribution occurs at a density of 0.5 (arbitrary units). (**G**) Raman spectroscopy maps of the relative nanotube density overlaid on an optical image of the 10-cm-wide SiO_2/Si wafer piece with TaFISA-aligned nanotubes deposited across. The ink is injected at position (i), and the flow is fully developed between regions (ii) and (iii). (**H**) Histogram of the relative density from the maps between positions (ii) and (iii) on the substrate. (**I**) SEM images of the aligned carbon nanotube film from approximate areas indicated across the sample. The scale bar in the right SEM image is 500 nm and applies to all SEM images in (I).

nanotube ordering and liquid crystal defects ($-^1/_2$ defect seen in Fig. 4B) observed at concentrations as low as 5 μg ml^{-1}. The onset of nematic assembly at orders of magnitude lower concentration than theory and past experiments is a result of the 2D confinement and accumulation of nanotubes at the liquid/liquid interface (*54*). At the onset of nematic ordering at ink concentration of 5 μg ml^{-1}, the areal density of nanotubes deposited is 26 $μm^{-2}$. This areal density matches predictions for the onset of nematic ordering for a 2D system of

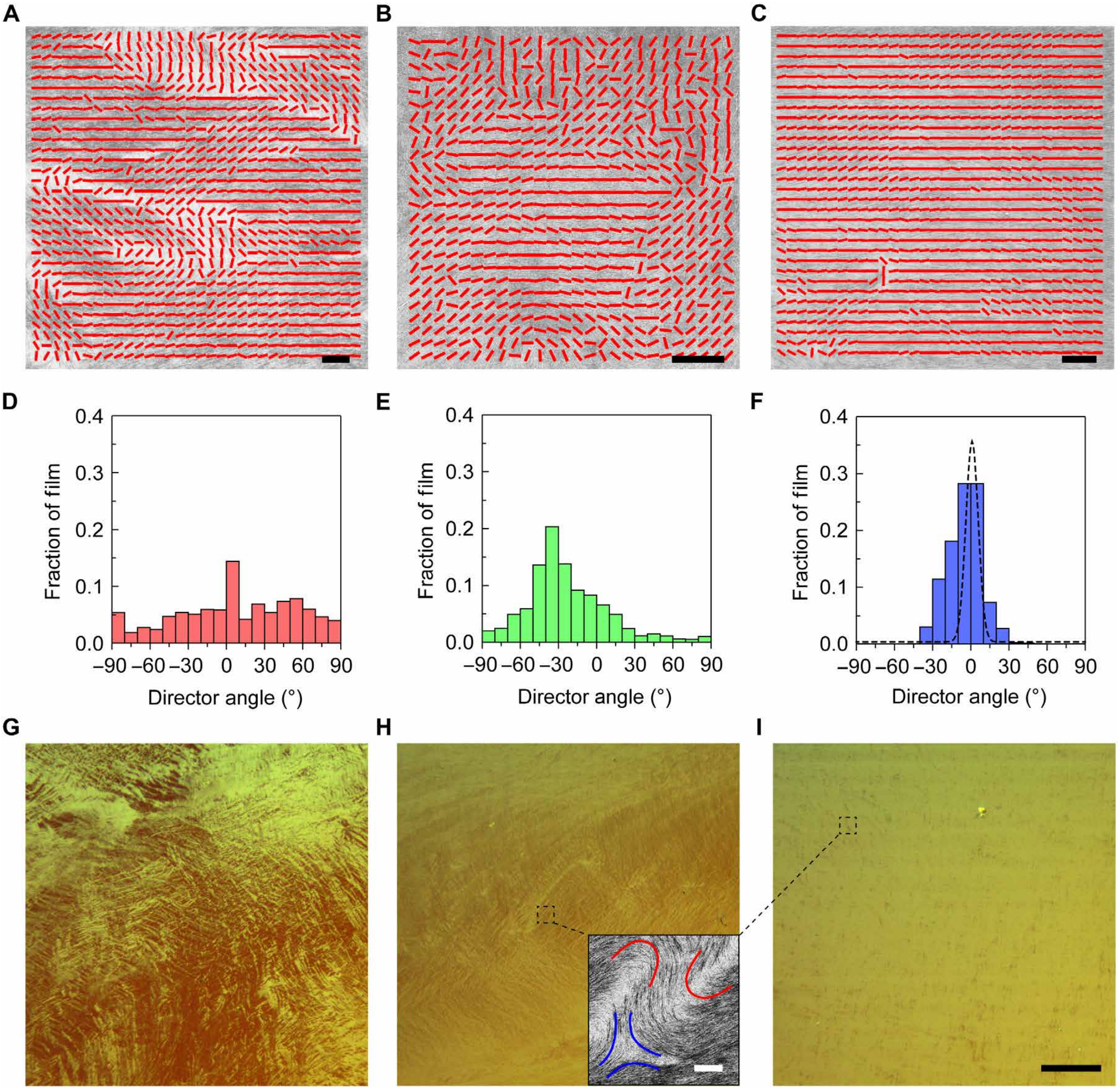

Fig. 3. Quantifying the effect of flow rate on ordering in TaFISA. (**A** to **C**) SEM images from TaFISA films fabricated with volumetric flow rates of 0, 1, and 4 ml min^{-1}, respectively, overlaid with local director orientations obtained from 2D fast Fourier transform analysis. Scale bars (A to C), 1 μm. Images without overlays are shown in fig. S5. (**D** to **F**) Director orientation distributions at flow rates of 0, 1, and 4 ml min^{-1}. The dashed line in (F) is the Gaussian fit of the local orientation histogram from Fig. 2B. (**G** to **I**) POM images from TaFISA films fabricated with volumetric flow rates of 0, 1, and 4 ml min^{-1}, respectively. Scale bar in (I) is 250 μm and applies to (G) to (I). SEM image inset in (H) shows $-^1/_2$ (blue) and $+^1/_2$ (red) liquid crystal defects in TaFISA films. Scale bar in inset, 2 μm.

rods (*54*) of 28 μm^{-2} (considering the dimensions of nanotubes used here, see calculation in the Supplementary Materials), further confirming the centrality of the 2D liquid/liquid interface and liquid crystal assembly in TaFISA.

The continuous arrays of well-aligned nanotubes assembled by TaFISA (at optimized flow rate and ink concentration) are punctuated only by small regions of disorder, such as liquid crystal defects. Decreasing temperature provides a route to suppress this disorder (*55*, *56*), for example, by reducing thermal motion and increasing the relative importance of anisotropic van der Waals interactions among mesogens (*47*). The substantial effect of temperature on TaFISA is clearly observed in the POM images presented in Fig. 4, which become notably more uniform by decreasing the temperature from 35°C (Fig. 4E) to 23°C (Fig. 4F) to 10°C (Fig. 4G). The figure insets quantify the distribution of POM pixel intensities, which converge to a uniform, tight distribution at 10°C, evidencing a substantial reduction in disorder and defects. The nanotube assemblies obtained at 10°C are highly ordered both on a large scale (0.7 mm by 0.7 mm area), as shown in Fig. 4G, and on a local scale, as shown in a corresponding SEM image in Fig. 4H.

FET measurements demonstrate that TaFISA arrays have excellent and uniform electrical characteristics (Figs. 5 and 6). FETs with 100- to 130-nm channel lengths are fabricated linearly across large-area assemblies of TaFISA nanotubes and, for comparison, FESA nanotubes as well. Representative source-drain current (I_{DS}) versus gate-source bias (V_{GS}) characteristics are shown in Fig. 5B for back-gated FETs, at a source-drain bias (V_{DS}) of −1 V. FETs fabricated from TaFISA arrays are shown in black, while FETs fabricated

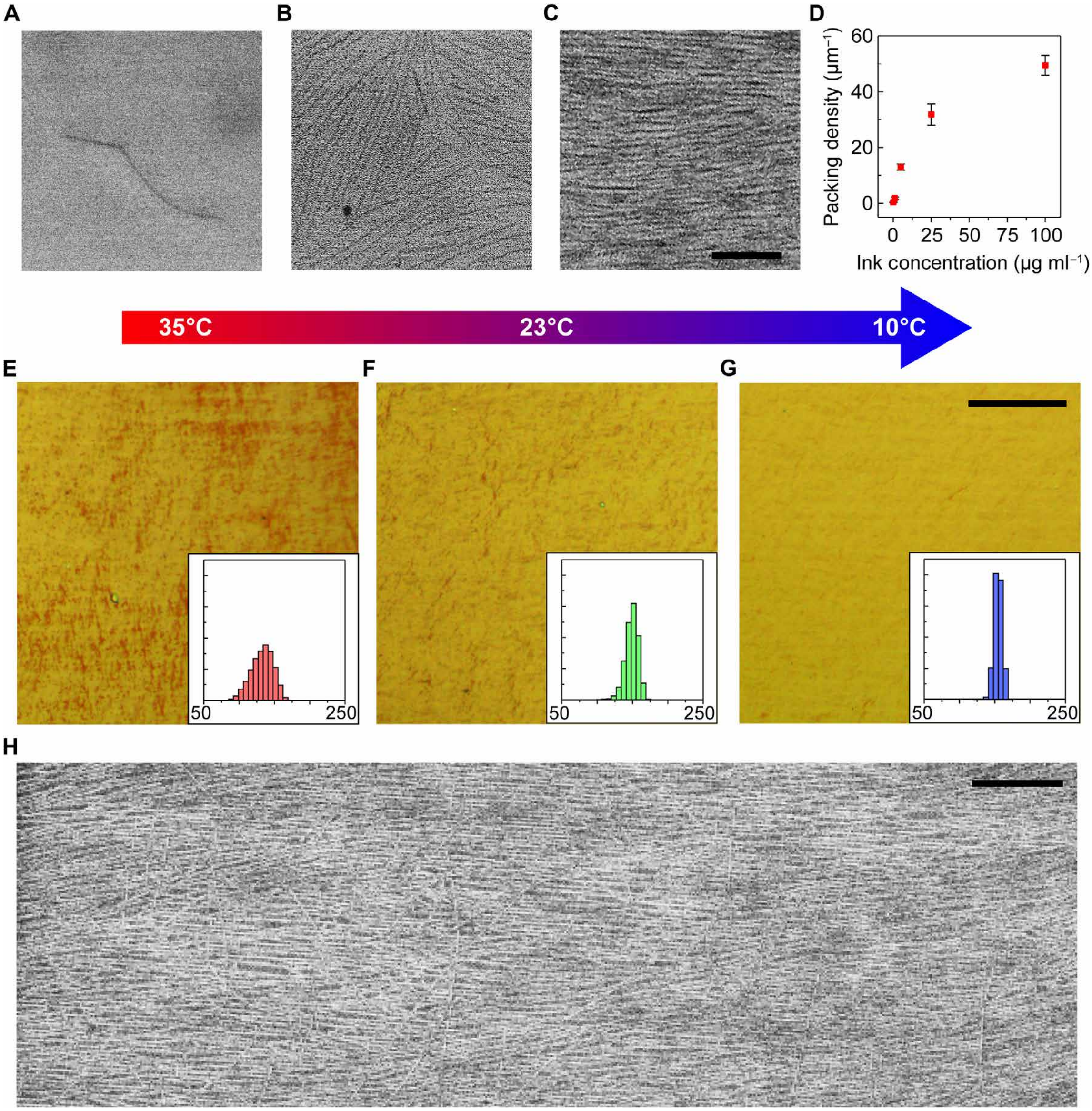

Fig. 4. Effect of concentration and temperature on TaFISA. (**A** to **C**) SEM images of TaFISA films fabricated using nanotube ink concentrations of 0.1, 5, and 100 μg ml^{-1}, respectively. The scale bar in (C) is 500 nm and applies to (A) to (C). (**D**) Packing density of resolvable rods as a function of bulk ink concentration. (**E** to **G**) POM images from TaFISA films deposited at 35°, 23°, and 10°C, respectively. The scale bar in (G) is 200 μm and applies to (E) to (G). To achieve temperatures of 35° and 10°C, the water subphase/trough is heated on a hot plate and placed in an ice bath, respectively. In (G), faint horizontal lines are spaced with a regular period of 29.6 μm. The substrate motor lift rate of 2670 μm s^{-1} divided by the line period corresponds to a frequency of 9.0×10^1 Hz, matching a frequency of 9.0×10^1 Hz inherent to the substrate lift motor control; therefore, these faint lines are artifacts. Histograms of POM image pixel intensity are shown in the insets in (E) to (G). (**H**) SEM image from the sample in (G). The measured packing density from SEM is 48 ± 2 μm^{-1}. Scale bar (H), 500 nm.

from FESA films are separately binned depending on whether the FETs are fabricated in aligned, stripe regions (red) or unaligned regions (blue).

The back-gated FETs (Fig. 5, A to C) turn on at negative V_{GS}, typical of p-type nanotube FETs with Pd source and drain contacts measured in ambient air on SiO_2. Using an ion gel top gate (Fig. 5, D and E) results in more ambipolar behavior, with an excellent subthreshold swing of 60 to 173 mV decade^{-1}, approaching the Boltzmann limit at room temperature of 60 mV decade^{-1}.

The Fig. 5B inset shows representative I_{DS} versus V_{DS} characteristics for back-gated TaFISA FETs, as V_{GS} is varied from −8 to −2 V. Typical on-state current densities reach 520 μA μm^{-1} (corresponding to 11 μA per nanotube) in TaFISA FETs at a V_{DS} of −0.6 V (at a channel length of 110 nm) and then saturate at more negative V_{DS}. In the linear regime at a small V_{DS} of −0.1 V, the typical on-state conductance is 1100 μS μm^{-1} (corresponding to 0.29 G_0 per nanotube, where $G_0 = 2e^2 h^{-1} = 77$ μS is the quantum conductance), demonstrating that charge transport in TaFISA arrays is approaching the quantum conductance limit of $2G_0$. The performance matches state-of-the-art FESA FETs (*40*), except TaFISA characteristics are uniformly obtained continuously across the substrate as opposed to selectively fabricated on well-ordered stripe regions as in FESA. The

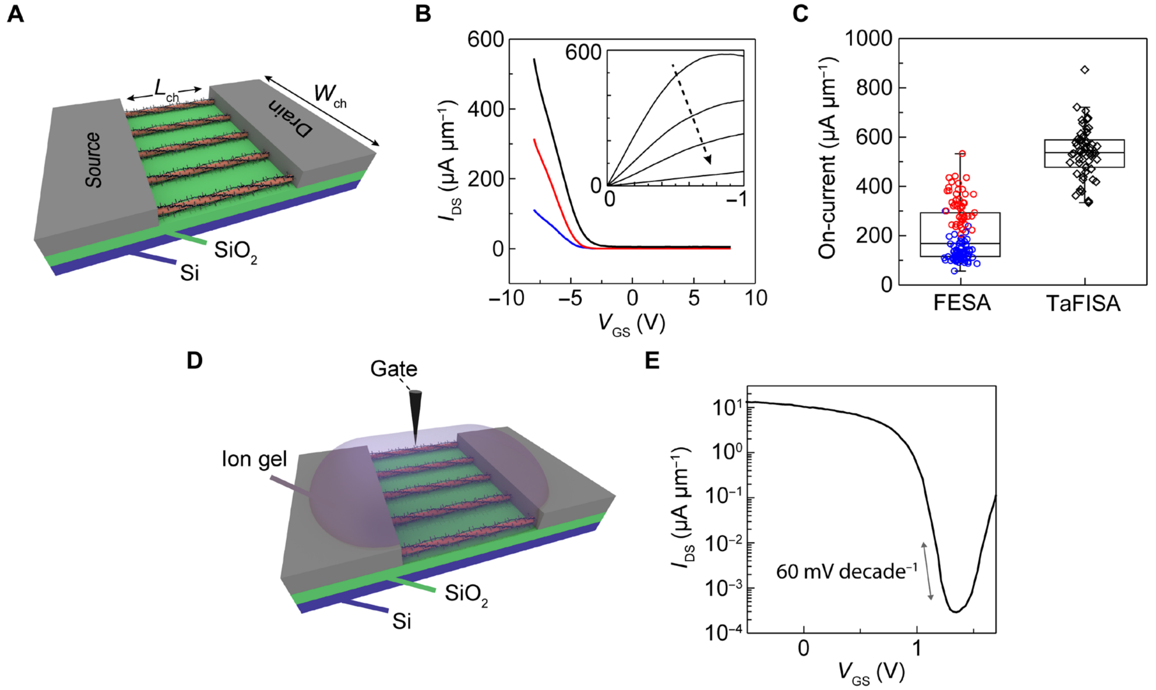

Fig. 5. Charge transport measurements of FETs fabricated on FESA and TaFISA carbon nanotube arrays. (**A**) Schematic of a nanotube array aligned on a SiO_2/Si back gate with top Pd source and drain contacts. (**B**) I_{DS} versus V_{GS} curves for representative back-gated TaFISA (black) and FESA (aligned, red; unaligned, blue) FETs. The on/off ratio is typically greater than 10^2 at a V_{DS} of −1 V. Inset: I_{DS} versus V_{DS} curves as V_{GS} is varied from −8 to −2 V (top to bottom) in 2-V steps. (**C**) On-current of all FESA and TaFISA FETs measured at a V_{DS} of −1 V. The lower on-current of the aligned FESA stripes compared to TaFISA arrays is attributed to a lower nanotube packing density of 38 ± 2 versus 50 ± 4 $μm^{-1}$ (data in terms of on-current per nanotube are shown in fig. S7). (**D**) Schematic of a nanotube array aligned on a SiO_2/Si substrate with ion gel top gate and Pd source and drain contacts. (**E**) I_{DS} versus V_{GS} curve for TaFISA arrays (nanotube packing density of 25 to 28 $μm^{-1}$) with ion gel top gate. This device exhibits a subthreshold swing of 60 mV $decade^{-1}$. The on/off ratio of FETs (L_{ch} = 130 nm) with an ion gel top gate is typically greater than 10^5 at a V_{DS} of −0.1 V.

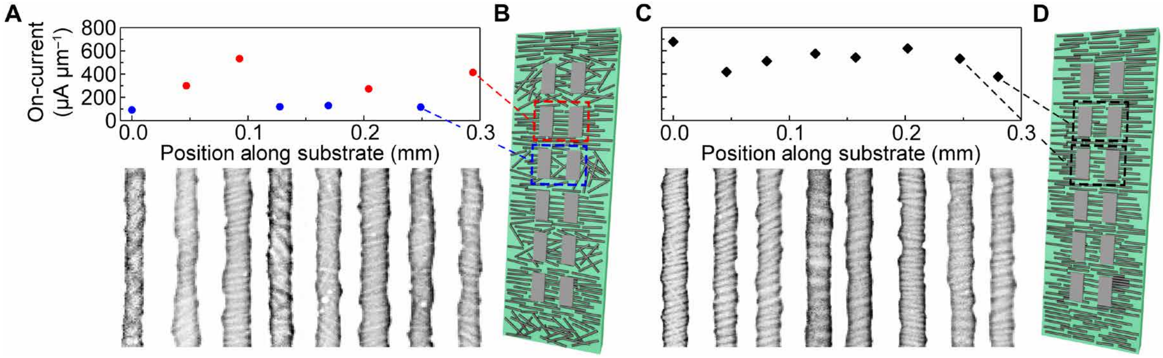

Fig. 6. Back-gated charge transport measurements of FESA and TaFISA carbon nanotube arrays correlated with array morphology. (**A**) On-current versus position across the substrate for selected individual FESA FETs. The channels of the FETs corresponding to each data point are shown directly below in the SEM images. From left to right, the channel lengths are 93, 100, 118, 115, 113, 124, 111, and 95 nm. (**B**) Schematic of FETs fabricated across FESA film. (**C**) On-current versus position along the substrate for individual TaFISA FETs. From left to right, the channel lengths are 114, 121, 126, 120, 101, 127, 129, and 134 nm. (**D**) Schematic of FETs fabricated across a TaFISA film. The effects of charging during SEM vary, causing the nanotubes to appear different in each SEM image.

on-state current and conductance moreover match or exceed state-of-the-art nanotube array FETs in the literature when gating efficiency is considered. For example, while (*13*) reaches an on-state current of 770 μA $μm^{-1}$ (at $V_{DS} = -0.6$ V and comparable gate length), it does so by using a much more efficient dielectric top gate to achieve a free carrier density in the nanotube channel that is several times higher. While gating efficiency is essential for obtaining high-performance circuits, it is largely an extrinsic parameter controlled by gate stack design that does not reflect the performance characteristics fundamental to a nanotube array. The comparable on-state current achieved here at several times lower charge density evidences the exceptional charge transport properties inherent to TaFISA-aligned arrays.

The FET-to-FET uniformity in on-current is quantified in Fig. 5C, for back-gated FETs, at $V_{DS} = -1$ V. Comparing all 58 TaFISA and

117 FESA devices measured (Fig. 5C), the TaFISA FETs demonstrate a mean normalized SD of only 19% (540 ± 100 μA μm^{-1}) as compared to 52% for FESA FETs (210 ± 110 μA μm^{-1}). The large variation in FESA FETs is a direct result of the stripe morphology—the devices fabricated on aligned regions (red), on average, exhibit 2.4× higher on-current than FETs fabricated on random regions (blue). Even in other implementations of FESA that have minimized the random regions, the variation in FET performance is large. For example, a mean normalized SD of 25% is obtained in (*43*) only after excluding most devices, which are lower performing.

The correlation between array morphology and FET performance is visualized in Fig. 6, in which nanotube morphology in the channel and on-current at $V_{DS} = -1$ V for the same back-gated FETs are directly compared. Disordered regions cause suppression of the on-current in FESA FETs, resulting in nonuniform electrical characteristics (Fig. 6, A and B). In contrast, on-current is consistent in TaFISA FETs because the channels are uniformly composed of aligned nanotubes, yielding more homogeneous FET performance (Fig. 6, C and D).

In addition to the superior electrical transport, the scalability of TaFISA is demonstrated by aligning nanotubes uniformly across the majority of a 10-cm-wide wafer piece (Fig. 2, G to I). The ink is injected in the channel at position (i). The flow develops between positions (i) and (ii) where few nanotubes are deposited. Between positions (ii) and (iii), the flow is developed, and aligned nanotubes are uniformly deposited onto the substrate as it is withdrawn from the water subphase. After position (iii), the flow is perturbed by end effects encountered at the edge of the wafer, related to the curvature of the water meniscus and divergence of the flow as it exits the channel. Raman spectroscopy maps of nanotube density are measured across the 10-cm-wide wafer and overlaid on a photograph of the wafer in Fig. 2G. The Raman maps demonstrate that the deposition is uniform across the region where the flow is fully developed (~60% of the wafer), confirming scalability. A histogram of the density analyzed between positions (ii) and (iii) is shown in Fig. 2H and shows that density varies with an HWHM of only 19%. SEM images (Fig. 2I) obtained across the substrate also confirm the continuous deposition of highly aligned, densely packed nanotubes.

DISCUSSION

These results demonstrate that carbon nanotubes collect and confine at a 2D liquid/liquid interface, self-organize via liquid crystal phenomena, and globally align with flow. The resulting nanotube assemblies can be transferred and deposited onto substrates to create wafer-scale arrays with exceptional local alignment (±6°). The high degree of local order (Fig. 2A) and birefringence (Fig. 3G) obtained without flow and without an external driving force to induce alignment, the strong dependence of ordering on concentration and temperature, and the observation of liquid crystal defects confirm the underlying role of liquid crystal phenomena in TaFISA. Moreover, the importance of the 2D liquid/liquid interface is evidenced by the excellent ordering obtained at nanotube ink concentrations much lower than bulk liquid crystal phase concentrations and at areal densities expected for 2D nematic ordering. Practically, the global alignment and uniformity improve with increasing flow rate up to 4 ml min^{-1}, increasing nanotube ink concentration up to 100 μg ml^{-1}, and decreasing temperature down to 10°C. The high degree of alignment and array uniformity lead to high on-state current densities averaging 520 μA μm^{-1} at −0.6 V and FET-to-FET variation of only 19%. Subthreshold swing measurements approaching the Boltzmann limit of 60 mV $decade^{-1}$ are achieved using an ion gel top gate, demonstrating the intrinsic quality of TaFISA nanotube arrays and the ability to efficiently modulate their conductivity with only small changes in gate potential.

The exploitation of TaFISA in future industrial processes will be facilitated by its continuous (e.g., continuously fed stream of wafers or continuous roll-to-roll deposition) nature, although full wafer coverage and more defect-free assembly will be needed. Full wafer coverage (as opposed to majority wafer coverage in Fig. 2G) should be viable by using wafer holders that allow the ink flow to fully develop before crossing the substrate and that control water meniscus curvature to avoid end effects. The coating of a 300-mm wafer in less than 2 min should be viable at a lift rate of 160 mm min^{-1}, the lift rate used in Figs. 2 (G to I) and 4 (A to D and E to H). At the same time, implementing the process in a cleanroom environment, taking measures to eliminate spurious particles and contaminants from the nanotube ink and aqueous subphase, and creating nanotube inks with more homogeneous nanotube populations that are free of short nanotube fragments and large nanotube aggregates [that can seed and stabilize liquid crystal defects (*34*, *49*, *50*)] are each expected to yield more uniform, defect-free assemblies. Engineering the polymer wrapper to suppress the formation of problematic nanotube aggregates, even at concentrations greater than 100 μg ml^{-1}, also has the potential to increase ordering while providing a route to higher nanotube packing densities. Further in situ studies of nanotube collection and ordering at the ink/water interface using interface-sensitive and polarization-dependent spectroscopies could shed light on the thermodynamics and kinetics of nanotube assembly at the 2D liquid/liquid interface and enable a deeper understanding of this powerful alignment phenomenon.

MATERIALS AND METHODS

Experimental design

A video of a typical TaFISA deposition and an additional simplified experimental schematic (fig. S10) are included in the Supplementary Materials. The TaFISA process is conducted using a channel, composed of a coplanar target substrate and a barrier (where the substrate and barrier are the same material with the same surface treatment; see the “Preparation of substrates” section below), that is attached to a substrate lift motor (Thorlabs, MTS50-Z8) and suspended in a trough filled with deionized (resistivity, ~18 megohms) water. Nanotube ink (polymer-wrapped carbon nanotubes suspended in an organic solvent) is injected into the channel using a needle, and the ink volumetric flow rate is controlled using a syringe pump (Chemyx, Nexus 3000). The needle is angled 15° from the horizontal, just slightly touching the surface of the water and roughly centered between the target substrate and barrier.

In the implementation of TaFISA studied, here, the channel is open at each end (i.e., at the entrance where the needle is inserted and the organic ink is introduced into the channel and also at the end of the substrate where the ink exits the channel). One implication of this open design is that while most of the ink flows down the length of the channel (i.e., away from the needle toward the exit), a small amount of ink escapes backward behind the needle. We find that the optimal channel width for this open-channel design is roughly 3 mm. If the channel is too wide (e.g., greater than 6 mm), then the ink velocity is too slow, causing the nanotube uniformity and alignment to decrease. If the channel width is too narrow (e.g., less than 2 mm), then the viscous friction in the channel is too large, and too much ink flows backward out the entrance side of the channel.

It is important to translate both the substrate and the barrier in parallel through the ink layer as it flows through the channel. If only the substrate is translated and the barrier remains stationary, the continuous accumulation of carbon nanotubes on the barrier becomes a problem and affects the ink flow and subsequent deposition. The channel lift rates used in this work, 26 to 160 mm min^{-1}, yield similar aligned nanotube deposition; however, qualitatively, at much higher lift rates (e.g., 2000 mm min^{-1}), the nanotube deposition decreases and becomes more disordered.

At the high ink flow rates that yield the best global alignment of nanotube domains (e.g., 4 ml min^{-1}; see Fig. 3), the ink layer translates more smoothly across the surface of the translating substrate (resulting in the deposition of more uniform assemblies of aligned nanotubes) when the substrate and channel are tilted (e.g., at 45° from the horizontal surface of the water trough). The experiments presented in Figs. 1 to 6 and figs. S1 to S9 use a channel oriented 45° from the horizontal. Figure S11 further elucidates the effect of channel tilt on nanotube deposition on both substrate and barrier. Specific experimental conditions for each figure are included in table S1.

Preparation of poly[(9,9-dioctylfluorenyl-2,7-diyl)-*alt-co*-(6,6′-{2,2′-bipyridine})]–wrapped semiconducting carbon nanotubes

Semiconducting carbon nanotubes are isolated from arc-discharge nanotube soot (Sigma-Aldrich, #698695) using a mass ratio (1:1) of the raw soot to polyfluorene derivative polymer wrapper, poly[(9,9-dioctylfluorenyl-2,7-diyl)-*alt-co*-(6,6′-{2,2′-bipyridine})] (PFO-BPy) (#ADS153-UV, American Dye Source Inc., Quebec, Canada). The PFO-BPy is first dispersed in toluene at a concentration of 2 mg ml^{-1} and is then combined with the nanotube soot and sonicated at 40% amplitude for 10 to 30 min using a horn-tip ultrasonicator (Sonic Dismembrator 500, Thermo Fisher Scientific, Waltham, MA). This solution is centrifuged (Sorvall WX, TH-641, Thermo Fisher Scientific) at $3 \times 10^5 g$ for 10 min to remove undispersed nanotubes and other amorphous carbon allotropes. The top 90% of the supernatant of each centrifuge tube is collected and filtered. The filtered supernatants are concentrated to a total volume of 60 ml using a rotary evaporator. This concentrated solution is centrifuged for 12 to 24 hours. The pellets are collected and then redispersed with fresh toluene. This centrifugation/redispersion process is repeated until the PFO-BPy:nanotube ratio is near 0.5:1 (4 to 10 repetitions). For the TaFISA alignment process, the pellets are then dispersed in chloroform (stabilized with ethanol from Thermo Fisher Scientific, #C606SK-1), and the concentration is measured optically. The nanotube concentration in solution is determined using known optical cross sections from the S_{22} transition (*40*, *57*).

An example optical absorption spectrum for the PFO-BPy–sorted arc-discharge carbon nanotubes used in this work is shown in fig. S12. After converting wavelength to energy, the S_{22} peak can be fit to a Gaussian distribution, and from this fit, we obtain a diameter distribution of 1.5 ± 0.2 nm, based on literature reference diameter-S_{22} data (*58*). Atomic force microscopy (AFM) measurements of nanotube diameters yields a diameter range of 1.3 ± 0.3 nm (example images shown in fig. S13), consistent with the diameters measured from optical absorption spectroscopy considering higher-order effects that skew AFM height data when there is surface energy contrast between nanostructure and substrate. Prior studies have established the semiconducting electronic-type purity of PFO-BPy–sorted arc-discharge nanotubes, prepared via the same methods as here, to be greater than 99.9% (*59*). The fact that there are so few metallic nanotubes in conjunction with the AFM measurements evidences that the nanotubes are effectively debundled during the sonication stage to allow metallic nanotubes to be removed during the centrifugation. Raman spectroscopy characterization of the nanotubes used in this work is shown in fig. S14. The Raman spectrum shows a large I_G/I_D ratio, indicating high-crystalline quality and low defect density.

Preparation of substrates

Highly p-type–doped Si wafers with 90 or 15 nm of dry, thermal oxide are used. The substrates are cleaned with a piranha solution with a 2:1 volume ratio of H_2SO_4 (91 to 92.5%):H_2O_2 (30%) in a crystallizing dish on a 110°C hot plate for 15 min (for 15-nm oxide) or 60 min (for 90-nm oxide), rinsed with deionized water, and dried with N_2. These piranha-cleaned wafers are baked for 335 s at 205°C and exposed to hexamethyldisilazane (HMDS) vapor (Solitec, VBS200 HMDS prime oven) for 2 to 10 s to achieve a water contact angle of 30° to 45°. If the water contact angle of the substrate is too low (e.g., less than 10°), then thick ropes of carbon nanotubes are deposited. As the substrate water contact angle increases (e.g., greater than 65°), the deposition on the target substrate becomes primarily random carbon nanotubes.

Fabrication of carbon nanotube FETs

After deposition of nanotubes on 15-nm SiO_2/Si substrates, 2 weight % polymethyl methacrylate is spin-cast at 3000 rpm for 90 s and then baked on a hot plate set at 185°C for 90 s. Electron-beam lithography is used to define the active channel areas (channel width, 4 μm), and the substrates are developed in 1:2 ratio of methyl isobutyl ketone to isopropyl alcohol by volume. Following a reactive ion etch to remove the nanotubes surrounding the active channel areas, the films are boiled in toluene to remove excess PFO-BPy and vacuum annealed at 400°C for 1 hour to decompose and remove the alkyl side chains of the PFO-BPy. Next, source and drain electrodes with a channel length of 100 to 120 nm are fabricated within the isolated regions of nanotubes via electron-beam lithography, development, and thermal deposition of 17.5 nm of Pd and 17.5 nm of Au. Back dielectric and top ionic liquid gate architectures are used to electrostatically control the FETs. The back gate architecture consists of 15-nm SiO_2 and Si substrate serving as the gate dielectric and gate electrode, respectively. One advantage of this back gate architecture is that it facilitates correlation between array morphology (via SEM) and electrical characteristics. While the relatively low capacitance of the 15-nm SiO_2 back gate challenges optimization of transconductance and subthreshold swing, these parameters can be largely improved by using thinner top gate dielectrics that increase the gate-channel capacitance (*60*) as opposed to improving nanotube alignment and ordering. The top gate architecture uses an ion gel prepared according to a previously published procedure (*61*). Briefly, the ionic liquid 1-ethyl-3-methylimidazolium bis(trifluoromethylsulphonyl)imide is initially dried under vacuum at 100°C for 3 days. The dried ionic liquid is fully mixed with polystyrene-*b*-poly(ethylene oxide)-*b*-polystyrene in dichloromethane to create the ion gel. The ion gel is spuncoat on samples at 4000 rpm to uniformly coat the entire substrate. During measurement, the gate probe is simply inserted into the gel near the FET being measured. The back-gated FETs exhibit hysteresis (fig. S8) as expected for FETs measured on SiO_2 in air, which has been previously attributed to adsorbed water and oxygen and/or charge traps in the oxide, while the ion gel top-gated FETs exhibit much lower hysteresis (fig. S9). Figure 5 (B and E) presents forward sweeps; both forward and backward sweeps are shown in figs. S8 and S9, respectively.

Raman spectroscopy

Raman spectroscopy (Thermo Fisher Scientific, DXRxi, 532-nm excitation laser wavelength) is used to map carbon nanotube density. The intensity of the G-band Raman mode is directly related to the density of carbon nanotubes on the substrate (assuming a spatially uniform chirality distribution) (*30*). Before Raman measurement, the carbon nanotube films are soaked in toluene at 120°C for 1 hour and then vacuum-annealed at 400°C for 1 hour. A Raman spectrum is collected at each pixel of the map, and the nanotube density is quantified by spectrally integrating over the G-band mode.

SUPPLEMENTARY MATERIALS

Supplementary material for this article is available at https://science.org/doi/10.1126/sciadv.abh0640

REFERENCES AND NOTES

1. G. S. Tulevski, A. D. Franklin, D. Frank, J. M. Lobez, Q. Cao, H. Park, A. Afzali, S.-J. Han, J. B. Hannon, W. Haensch, Toward high-performance digital logic technology with carbon nanotubes. *ACS Nano* **8**, 8730–8745 (2014).
2. A. D. Franklin, M. Luisier, S.-J. Han, G. Tulevski, C. M. Breslin, L. Gignac, M. S. Lundstrom, W. Haensch, Sub-10 nm carbon nanotube transistor. *Nano Lett.* **12**, 758–762 (2012).
3. C. Qiu, Z. Zhang, M. Xiao, Y. Yang, D. Zhong, L.-M. Peng, Scaling carbon nanotube complementary transistors to 5-nm gate lengths. *Science* **355**, 271–276 (2017).
4. K. R. Jinkins, J. Chan, R. M. Jacobberger, A. Berson, M. S. Arnold, Substrate-wide confined shear alignment of carbon nanotubes for thin film transistors. *Adv. Electron. Mater.* **5**, 1800593 (2019).
5. Y. Huang, X. Duan, Q. Wei, C. M. Lieber, Directed assembly of one-dimensional nanostructures into functional networks. *Science* **291**, 630–633 (2001).
6. X. He, W. Gao, L. Xie, B. Li, Q. Zhang, S. Lei, J. M. Robinson, E. H. Hároz, S. K. Doorn, W. Wang, R. Vajtai, P. M. Ajayan, W. W. Adams, R. H. Hauge, J. Kono, Wafer-scale monodomain films of spontaneously aligned single-walled carbon nanotubes. *Nat. Nanotech.* **11**, 633–638 (2016).
7. J. Hedberg, L. Dong, J. Jiao, Air flow technique for large scale dispersion and alignment of carbon nanotubes on various substrates. *Appl. Phys. Lett.* **86**, 143111 (2005).
8. M. D. Lay, J. P. Novak, E. S. Snow, Simple route to large-scale ordered arrays of liquid-deposited carbon nanotubes. *Nano Lett.* **4**, 603–606 (2004).
9. A. Vijayaraghavan, S. Blatt, D. Weissenberger, M. Oron-Carl, F. Hennrich, D. Gerthsen, H. Hahn, R. Krupke, Ultra-large-scale directed assembly of single-walled carbon nanotube devices. *Nano Lett.* **7**, 1556–1560 (2007).
10. H. Shimoda, S. J. Oh, H. Z. Geng, R. J. Walker, X. B. Zhang, L. E. McNeil, O. Zhou, Self-assembly of carbon nanotubes. *Adv. Mater.* **14**, 899–901 (2002).
11. M. Engel, J. P. Small, M. Steiner, M. Freitag, A. A. Green, M. C. Hersam, P. Avouris, Thin film nanotube transistors based on self-assembled, aligned, semiconducting carbon nanotube arrays. *ACS Nano* **2**, 2445–2452 (2008).
12. J. Si, D. Zhong, H. Xu, M. Xiao, C. Yu, Z. Zhang, L.-M. Peng, Scalable preparation of high-density semiconducting carbon nanotube arrays for high-performance field-effect transistors. *ACS Nano* **12**, 627–634 (2018).
13. L. Liu, J. Han, L. Xu, J. Zhou, C. Zhao, S. Ding, H. Shi, M. Xiao, L. Ding, Z. Ma, C. Jin, Z. Zhang, L.-M. Peng, Aligned, high-density semiconducting carbon nanotube arrays for high-performance electronics. *Science* **368**, 850–856 (2020).
14. W. Sun, J. Shen, Z. Zhao, N. Arellano, C. Rettner, J. Tang, T. Cao, Z. Zhou, T. Ta, J. K. Streit, J. A. Fagan, T. Schaus, M. Zheng, S.-J. Han, W. M. Shih, H. T. Maune, P. Yin, Precise pitch-scaling of carbon nanotube arrays within three-dimensional DNA nanotrenches. *Science* **368**, 874–877 (2020).
15. M. Zhao, Y. Chen, K. Wang, Z. Zhang, J. K. Streit, J. A. Fagan, J. Tang, M. Zheng, C. Yang, Z. Zhu, W. Sun, DNA-directed nanofabrication of high-performance carbon nanotube field-effect transistors. *Science* **368**, 878–881 (2020).
16. X. Li, L. Zhang, X. Wang, I. Shimoyama, X. Sun, W.-S. Seo, H. Dai, Langmuir–Blodgett assembly of densely aligned single-walled carbon nanotubes from bulk materials. *J. Am. Chem. Soc.* **129**, 4890–4891 (2007).
17. V. Sgobba, G. Giancane, D. Cannoletta, A. Operamolla, O. Hassan Omar, G. M. Farinola, D. M. Guldi, L. Valli, Langmuir–Schaefer films for aligned carbon nanotubes functionalized with a conjugate polymer and photoelectrochemical response enhancement. *ACS Appl. Mater. Interfaces* **6**, 153–158 (2014).
18. F. Léonard, Crosstalk between nanotube devices: Contact and channel effects. *Nanotechnology* **17**, 2381–2385 (2006).
19. W. H. Binder, Supramolecular assembly of nanoparticles at liquid–liquid interfaces. *Angew. Chem. Int. Ed.* **44**, 5172–5175 (2005).
20. K. Schwenke, L. Isa, E. Del Gado, Assembly of nanoparticles at liquid interfaces: Crowding and ordering. *Langmuir* **30**, 3069–3074 (2014).
21. Y. Zhang, L. Xu, W. R. Walker, C. M. Tittle, C. J. Backhouse, M. A. Pope, Langmuir films and uniform, large area, transparent coatings of chemically exfoliated MoS_2 single layers. *J. Mater. Chem. C* **5**, 11275–11287 (2017).
22. S. J. DeCamp, G. S. Redner, A. Baskaran, M. F. Hagan, Z. Dogic, Orientational order of motile defects in active nematics. *Nat. Mater.* **14**, 1110–1115 (2015).
23. S. Jordens, L. Isa, I. Usov, R. Mezzenga, Non-equilibrium nature of two-dimensional isotropic and nematic coexistence in amyloid fibrils at liquid interfaces. *Nat. Commun.* **4**, 1917 (2013).
24. J. Matsui, K. Yamamoto, N. Inokuma, H. Orikasa, T. Kyotani, T. Miyashita, Fabrication of densely packed multi-walled carbon nanotube ultrathin films using a liquid–liquid interface. *J. Mater. Chem.* **17**, 3806 (2007).
25. J. Matsui, M. Iko, N. Inokuma, H. Orikasa, M. Mitsuishi, T. Kyotani, T. Miyashita, Simple fabrication of carbon nanotube monolayer film. *Chem. Lett.* **35**, 42–43 (2006).
26. H. Wang, E. K. Hobbie, Amphiphobic carbon nanotubes as macroemulsion surfactants. *Langmuir* **19**, 3091–3093 (2003).
27. Y. Zhang, Y. Shen, D. Kuehner, S. Wu, Z. Su, S. Ye, L. Niu, Directing single-walled carbon nanotubes to self-assemble at water/oil interfaces and facilitate electron transfer. *Chem. Commun.* **2008**, 4273 (2008).
28. T. Feng, D. A. Hoagland, T. P. Russell, Assembly of acid-functionalized single-walled carbon nanotubes at oil/water interfaces. *Langmuir* **30**, 1072–1079 (2014).
29. J. Matsui, K. Yamamoto, T. Miyashita, Assembly of untreated single-walled carbon nanotubes at a liquid–liquid interface. *Carbon* **47**, 1444–1450 (2009).
30. S. Zhang, S. Kumar, Carbon nanotubes as liquid crystals. *Small* **4**, 1270–1283 (2008).
31. B. King, B. Panchapakesan, Vacuum filtration based formation of liquid crystal films of semiconducting carbon nanotubes and high performance transistor devices. *Nanotechnology* **25**, 175201 (2014).
32. O. Kleinerman, L. Liberman, N. Behabtu, M. Pasquali, Y. Cohen, Y. Talmon, Direct imaging of carbon nanotube liquid-crystalline phase development in true solutions. *Langmuir* **33**, 4011–4018 (2017).
33. H. W. Lee, W. You, S. Barman, S. Hellstrom, M. C. LeMieux, J. H. Oh, S. Liu, T. Fujiwara, W. M. Wang, B. Chen, Y. W. Jin, J. M. Kim, Z. Bao, Lyotropic liquid-crystalline solutions of high-concentration dispersions of single-walled carbon nanotubes with conjugated polymers. *Small* **5**, 1019–1024 (2009).
34. S. Zhang, I. A. Kinloch, A. H. Windle, Mesogenicity drives fractionation in lyotropic aqueous suspensions of multiwall carbon nanotubes. *Nano Lett.* **6**, 568–572 (2006).
35. S. Badaire, C. Zakri, M. Maugey, A. Derré, J. N. Barisci, G. Wallace, P. Poulin, Liquid crystals of DNA-stabilized carbon nanotubes. *Adv. Mater.* **17**, 1673–1676 (2005).
36. H. Ko, V. V. Tsukruk, Liquid-crystalline processing of highly oriented carbon nanotube arrays for thin-film transistors. *Nano Lett.* **6**, 1443–1448 (2006).
37. R. S. Mclean, X. Huang, C. Khripin, A. Jagota, M. Zheng, Controlled two-dimensional pattern of spontaneously aligned carbon nanotubes. *Nano Lett.* **6**, 55–60 (2006).
38. K. R. Jinkins, J. Chan, G. J. Brady, K. K. Gronski, P. Gopalan, H. T. Evensen, A. Berson, M. S. Arnold, Nanotube alignment mechanism in floating evaporative self-assembly. *Langmuir* **33**, 13407–13414 (2017).
39. Y. Joo, G. J. Brady, M. S. Arnold, P. Gopalan, Dose-controlled, floating evaporative self-assembly and alignment of semiconducting carbon nanotubes from organic solvents. *Langmuir* **30**, 3460–3466 (2014).
40. G. J. Brady, A. J. Way, N. S. Safron, H. T. Evensen, P. Gopalan, M. S. Arnold, Quasi-ballistic carbon nanotube array transistors with current density exceeding Si and GaAs. *Sci. Adv.* **2**, e1601240 (2016).
41. G. J. Brady, K. R. Jinkins, M. S. Arnold, Channel length scaling behavior in transistors based on individual versus dense arrays of carbon nanotubes. *J. Appl. Phys.* **122**, 124506 (2017).
42. Y. Cao, G. J. Brady, H. Gui, C. Rutherglen, M. S. Arnold, C. Zhou, Radio frequency transistors using aligned semiconducting carbon nanotubes with current-gain cutoff frequency and maximum oscillation frequency simultaneously greater than 70 GHz. *ACS Nano* **10**, 6782–6790 (2016).

43. C. Rutherglen, A. A. Kane, P. F. Marsh, T. A. Cain, B. I. Hassan, M. R. AlShareef, C. Zhou, K. Galatsis, Wafer-scalable, aligned carbon nanotube transistors operating at frequencies of over 100 GHz. *Nat. Electron.* **2**, 530–539 (2019).
44. F. Mirri, A. W. K. Ma, T. T. Hsu, N. Behabtu, S. L. Eichmann, C. C. Young, D. E. Tsentalovich, M. Pasquali, High-performance carbon nanotube transparent conductive films by scalable dip coating. *ACS Nano* **6**, 9737–9744 (2012).
45. L. Xiang, F. Xia, W. Jin, X. Zeng, F. Liu, X. Liang, Y. Hu, Carbon nanotube dual-material gate devices for flexible configurable multifunctional electronics. *Carbon* **161**, 656–664 (2020).
46. E. Brandley, E. S. Greenhalgh, M. S. P. Shaffer, Q. Li, Mapping carbon nanotube orientation by fast fourier transform of scanning electron micrographs. *Carbon* **137**, 78–87 (2018).
47. R. G. Larson, *The Structure and Rheology of Complex Fluids* (Oxford Univ. Press Inc., ed. 1, 1999), pp. 443–502.
48. R. G. Larson, D. W. Mead, The Ericksen number and Deborah number cascades in sheared polymeric nematics. *Liq. Cryst.* **15**, 151–169 (1993).
49. L. Lu, W. Chen, Large-scale aligned carbon nanotubes from their purified, highly concentrated suspension. *ACS Nano* **4**, 1042–1048 (2010).
50. W. Song, A. H. Windle, Size-dependence and elasticity of liquid-crystalline multiwalled carbon nanotubes. *Adv. Mater.* **20**, 3149–3154 (2008).
51. C. Zakri, C. Blanc, E. Grelet, C. Zamora-Ledezma, N. Puech, E. Anglaret, P. Poulin, Liquid crystals of carbon nanotubes and graphene. *Phil. Trans. R. Soc. A* **371**, 20120499 (2013).
52. L. Onsager, The effects of shape on the interaction of colloidal particles. *Ann. N. Y. Acad. Sci.* **51**, 627–659 (1949).
53. A. R. Khokhlov, A. N. Semenov, Liquid-crystalline ordering in the solution of long persistent chains. *Physica A* **108**, 546–556 (1981).
54. A. Czogalla, D. J. Kauert, R. Seidel, P. Schwille, E. P. Petrov, DNA origami nanoneedles on freestanding lipid membranes as a tool to observe isotropic–nematic transition in two dimensions. *Nano Lett.* **15**, 649–655 (2015).
55. M.-R. Puica, Lyotropic liquid crystals at phase transitions. *Romanian Rep. Phys.* **58**, 491–518 (2006).
56. D. Andrienko, Introduction to liquid crystals. *J. Mol. Liq.* **267**, 520–541 (2018).
57. K. S. Mistry, B. A. Larsen, J. L. Blackburn, High-yield dispersions of large-diameter semiconducting single-walled carbon nanotubes with tunable narrow chirality distributions. *ACS Nano* **7**, 2231–2239 (2013).
58. R. B. Weisman, S. M. Bachilo, Dependence of optical transition energies on structure for single-walled carbon nanotubes in aqueous suspension: An empirical Kataura plot. *Nano Lett.* **3**, 1235–1238 (2003).
59. G. J. Brady, Y. Joo, S. Singha Roy, P. Gopalan, M. S. Arnold, High performance transistors via aligned polyfluorene-sorted carbon nanotubes. *Appl. Phys. Lett.* **104**, 083107 (2014).
60. J. Appenzeller, J. Knoch, R. Martel, V. Derycke, S. J. Wind, P. Avouris, Carbon nanotube electronics. *IEEE Trans. Nanotechnol.* **1**, 184–189 (2002).
61. C.-F. Chen, C.-H. Park, B. W. Boudouris, J. Horng, B. Geng, C. Girit, A. Zettl, M. F. Crommie, R. A. Segalman, S. G. Louie, F. Wang, Controlling inelastic light scattering quantum pathways in graphene. *Nature* **471**, 617–620 (2011).
62. M. A. Bates, D. Frenkel, Phase behavior of two-dimensional hard rod fluids. *J. Chem. Phys.* **112**, 10034–10041 (2000).
63. D. Frenkel, R. Eppenga, Evidence for algebraic orientational order in a two-dimensional hard-core nematic. *Phys. Rev. A* **31**, 1776–1787 (1985).

Acknowledgments: We acknowledge the use of facilities and instrumentation supported by NSF through the University of Wisconsin Materials Research Science and Engineering Center (DMR-1121288, 0079983, and 0520057) and through the University of Wisconsin Nanoscale Science and Engineering Center (DMR-0832760 and 0425880). In addition, we acknowledge the use of the DXRxi Raman spectrometer at Thermo Fisher Scientific. **Funding:** This work was supported by NSF-Scalable Nanomanufacturing grant 1727523 (to K.R.J., S.M.F., J.H.D., P.G., A.B., and M.S.A.), NSF Division of Graduate Education grant 1256259 (to K.R.J.), and U.S. Department of Energy, Office of Science, Basic Energy Sciences grant DE-SC0016007 (to V.S. and R.M.J.). **Author contributions:** Discovery of TaFISA: K.R.J., P.G., and M.S.A. TaFISA nanotube assembly, characterization, and scaling; FESA experiments; and back-gated FET fabrication and characterization: K.R.J. Ion gel top gate FET fabrication and characterization: S.M.F. Ion gel preparation: J.H.D. Fast Fourier transform analysis: A.B., K.R.J., and M.S.A. Graphene fabrication for Raman normalization: V.S. Thermal annealing of nanotube arrays for FETs: R.M.J. Manuscript preparation: led by K.R.J. and M.S.A., with contributions from all authors. **Competing interests:** "Alignment of carbon nanotubes in confined channels" (U.S. patent no. US10873026B2). U.S. Patent and Trademark Office (2020) (K.R.J., P.G., and M.S.A.). All other authors declare that they have no competing interests. **Data and materials availability:** All data needed to evaluate the conclusions in the paper are present in the paper and/or the Supplementary Materials.

Submitted 14 February 2021
Accepted 20 July 2021
Published 8 September 2021
10.1126/sciadv.abh0640

Citation: K. R. Jinkins, S. M. Foradori, V. Saraswat, R. M. Jacobberger, J. H. Dwyer, P. Gopalan, A. Berson, M. S. Arnold, Aligned 2D carbon nanotube liquid crystals for wafer-scale electronics. *Sci. Adv.* **7**, eabh0640 (2021).

Science Advances

Aligned 2D carbon nanotube liquid crystals for wafer-scale electronics

Katherine R. JinkinsSean M. ForadoriVivek SaraswatRobert M. JacobbergerJonathan H. DwyerPadma GopalanArganthaël BersonMichael S. Arnold

Sci. Adv., 7 (37), eabh0640. • DOI: 10.1126/sciadv.abh0640

Science Advances (ISSN) is published by the American Association for the Advancement of Science. 1200 New York Avenue NW, Washington, DC 20005. The title *Science Advances* is a registered trademark of AAAS.